Materials Science & Engineering C 107 (2020) 110305

Contents lists available at ScienceDirect

Materials Science & Engineering C

journal homepage: www.elsevier.com/locate/msec

An assessment of biomedical CoCrMo alloy fabricated by direct metal laser sintering technique for implant applications

Daniel de Castro Girão[a,*], Miloslav Béreš[a,b], André Luiz Jardini[b], Rubens Maciel Filho[b], Cleiton Carvalho Silva[a], Abner de Siervo[c], Hamilton Ferreira Gomes de Abreu[a], Walney Silva Araújo[a]

[a] Department of Metallurgical and Materials Engineering, Universidade Federal do Ceará, 60440-900, Fortaleza, CE, Brazil
[b] BIOFABRIS - National Institute of Science and Technology in Biomanufacturing, Faculty of Chemical Engineering, University of Campinas, 13081-970, Campinas, SP, Brazil
[c] Institute of Physics "Gleb Wataghin", University of Campinas, 13083-859, Campinas, SP, Brazil

ARTICLE INFO

Keywords:
CoCrMo alloy
Corrosion resistance
Simulated body fluids
Additive manufacturing
Direct metal laser sintering

ABSTRACT

CoCrMo alloys have been used for several decades in implantable devices due to their favourable mechanical properties, low wear rate in addition to good biocompatibility and high corrosion resistance. These alloys are conventionally produced via casting and/or forging route, however additive manufacturing techniques being recently employed in their fabrication. In this work, CoCrMo samples were produced by direct metal laser sintering additive manufacturing process. The microstructure and surface composition were examined employing scanning electron microscopy, X-ray diffraction and X-ray photoelectron spectroscopy (XPS). The corrosion resistance was measured in 0.14 M sodium chloride solution and in phosphate buffered solution (PBS) both with and without addition of albumin at pH 7.4 and 37 °C. For this, potentiodynamic tests in addition to electrochemical impedance spectroscopy were employed. The studied CoCrMo alloy exhibits a good corrosion resistance in solutions tested being the highest in PBS solution without albumin addition. The XPS analysis showed that the passive film composition and its thickness are not modified by the adsorbed layer. Microstructural analysis revealed occurrence of strain-induced martensitic transformation.

1. Introduction

For more than five decades, cobalt-chromium-molybdenum (CoCrMo) alloys have been used in the cast or wrought form as prosthetic [1,2] or dental implant materials due to their favourable mechanical properties, low wear in addition to good biocompatibility and high corrosion resistance [3]. The latter is based on a passive oxide film that forms on the metal surface within human body environment [4]. This oxide film consists of a mix of cobalt, chromium and molybdenum oxides, mainly Cr_2O_3 [5] which plays two roles in limiting both the anodic and cathodic reactions, serving as a physical barrier for cation and anion transport to the metal surface as well as electronic barrier for electrons [3]. An exposure to corrosive biological fluids unavoidably causes corrosion of an implant to some level. The prevailing corrosion mechanism of CoCrMo alloys is believed to be passive dissolution, where metal ions migrates through passive oxide layer [6]. During long-term exposure of the implanted material to human body fluids, the oxide film may be disrupted by either chemical reaction or mechanical wear and metal ions that are released could be harmful to human health [7]. It is estimated that approximately 20% of patients with well-functioning implants and 60% of patients with poorly functioning implants develop metal hypersensitivity reactions which can be attributed to metal ion release [8]. In addition, carcinogenicity and toxicity of this alloy system is still subject of discussion [9,10]. The corrosion rates of CoCrMo alloys are usually analysed *in vitro* using simulated body fluids, which typically include bovine calf serum, phosphate buffered solution, sodium chloride solution, Hank solution and Ringer solution. Also, animal or human synovial fluids are used to study corrosion mechanism *in vivo* or *in vitro* [6].

Casting, machining and plastic work fabrication processes are well established techniques to produce CoCrMo alloys. Due to the technical difficulties by fabrication, which are caused by the high hardness of the material, strain hardening, increased tool and machine wear, alternative cost effective production routes are needed. Emerging additive manufacturing (AM) technologies, including powder bed systems, powder feed systems and wire feed systems [11], can on the one hand

* Corresponding author.
E-mail address: danielcg@alu.ufc.br (D. de Castro Girão).

https://doi.org/10.1016/j.msec.2019.110305
Received 11 October 2017; Received in revised form 22 June 2018; Accepted 11 October 2019
Available online 21 October 2019
0928-4931/

simplify the fabrication route, reduce total cost and offers possibility of production of customised implants [12]. On the other hand, component certification and process qualification standards for AM parts are not completely elaborated yet [13]. To date, there have been only limited number of studies that analyse corrosion resistance of CoCrMo alloys fabricated via AM route [14]. In ref. [10], the susceptibility for corrosion and metal release increased with an increased number melt pool boundaries. Study of Lu *et al.* [14] revealed that laser beam scanning strategy can alter the corrosion resistance of the finished part. The difference in corrosion resistance was attributed to the thermal residual stress that occurs during fabrication. The objective of the present study is to examine the corrosion susceptibility of this alloy system fabricated via powder bed direct metal laser sintering technique (DMLS). In this process, a heat source fuses metal powder in layer-by-layer manner to form the desired part, which is defined by a CAD model. In the present work, we examine the electrochemical behaviour of DMLS fabricated samples in phosphate buffered solution (PBS) in addition to sodium chloride solution both with and without addition of albumin. In this regard, electrochemical tests were conducted which consisted of open circuit potential, impedance spectroscopy and potentiodynamic polarisation measurements.

2. Material and experimental procedure

CoCrMo samples were produced by DMLS process using Eosint EOS M280 machine for both corrosion tests and microstructural analysis (dimension of $10 \times 10 \times 10\ mm^3$) in addition to tensile test specimens with cross-section of $3.5 \times 1.5\ mm^2$. Samples were fabricated from pre-alloyed gas atomised CoCrMo powder (EOS Cobalt/Chrome MP1), supplied by Eosint GmbH, Germany. A continuous laser beam-scanning mode was employed and manufacturer's recommended parameters were applied. The laser sintered specimens were prepared and examined in the as-received condition parallel to the build direction plane.

2.1. X-ray diffraction (XRD)

XRD technique was used to identify phases present in both the precursor powder and in the laser sintered specimens. Prior to the measurement of the laser sintered samples, the surfaces of two different specimens were prepared. The first sample was ground with 1200 grit SiC paper (depicted as “ground”) whereas second specimen was prepared by electropolishing (depicted as “electropolished”), using a mixture of 5 vol.- % perchloric acid in acetic acid under applied voltage of 25V. The prepared samples were rinsed in distilled water and ethanol. XRD measurements in the angular range $2\theta = 30–90^\circ$ were carried out using a Philips® X'Pert Pro diffractometer. Cu Kα radiation source (wavelength of 0.154 nm) was used with applied voltage and current of 40 kV and 45 mA, respectively. The obtained diffraction patterns were compared with data from the ICSD database in order to identify phases present.

2.2. Synchrotron X-ray diffraction

Synchrotron X-ray diffraction was used to follow the strain-induced martensitic transformation in the laser sintered specimens during tensile loading at room temperature. The electropolished tensile test specimen with cross-section of $3.5 \times 1.5\ mm^2$ was strained to failure in the Gleeble Thermomechanical Simulator integrated within the XTMS beamline at the Brazilian Synchrotron Light Laboratory, Campinas, Brazil. The tensile specimen was positioned perpendicular to the diffraction beam and then loaded under tension at a constant cross-head displacement rate of $1 \times 10^{-3}\ mm.s^{-1}$. The projection of sample cross-section at the gauge centre was recorded by a laser dilatometer. The Gleeble system operated in stroke control mode and the macroscopic force applied to the sample was registered using a 44 kN load cell. A monochromatic X-ray beam with dimensions at the slit system of $2.0 \times 0.5\ mm^2$ and wavelength of 1.0332 Å (12 keV) was used to illuminate the sample. During loading, diffraction data were collected at 3 s intervals using two silicon microstrips MYTHEN one-dimensional detectors. As result, the time-resolved diffraction data were plotted in an intensity colour map to qualitatively demonstrate the strain-induced transformation using a custom peak-fitting algorithm developed for the IgorPro software by Babu *et al.* [15].

2.3. Microstructural characterisation

Samples for electron backscattered diffraction (EBSD) analysis were prepared by polishing with a set of decreasing size diamond suspensions down to 1 μm. Final polishing step was conducted on Buehler MiniMet™ Polisher using colloidal silica for duration of several hours. EBSD analysis was performed employing FEI Quanta 450 and FEI Quanta 650 scanning electron microscopes (SEM) equipped with HKL Nordlys orientation imaging system (Oxford Instruments, Oxford, UK). The HKL Channel 5 software package (Oxford Instruments, Oxford, UK) was used to process the EBSD data. In addition, specimens for microstructural characterisation were electropolished using solution of 5 vol.-% concentrated perchloric acid in an acetic acid base electrolyte under applied voltage of 21 V and temperature of 15 °C, respectively. These samples were examined by secondary electron imaging using FEI Quanta 450 SEM.

2.4. Electrochemical tests

To analyse corrosion behaviour of the CoCrMo alloy, electrochemical tests were carried out using four different solutions including: (i) 0.14 M NaCl, (ii) 0.14 M NaCl with 0.5 g/L of albumin, (iii) PBS solution (0.14 M NaCl, 1 mM KH_2PO_4, 3 mM KCl and 10 mM Na_2HPO_4) and finally (iv) PBS with 0.5 g/L of albumin, where solutions (iii) and (iv) are tagged as simulated body fluids. Selected solutions evaluate the influence of albumin, chloride and phosphate ions on the electrochemical behaviour of the laser sintered material and compare its corrosion resistance with conventionally produced alloy previously examined in ref. [16]. The pH values of the non-buffered solutions were adjusted to pH 7.4 at 37 °C with addition of concentrated HCl or concentrated NaOH before each experiment.

The CoCrMo sample was embedded into non-conductive resin and area of $0.30\ cm^2$ was selected using enamel varnish for electrochemical tests. Prior to each experiment, the sample was initially ground with 1200 grit SiC paper, then degreased with ethanol and washed with deionised water and finally dried with compressed air.

Electrochemical tests were performed using Potentiostat PGSTAT302 N (Metrohm Autolab B.V.) equipment operated by NOVA software v. 1.11.0. A double-wall three-electrode cell (volume of 100 mL) in aerated conditions under constant magnetic stirring was used for all electrochemical measurements. An Ag/AgCl 3 M KCl reference electrode and a Pt wire were used as the counter electrode. In order to reach a stable state of the electrochemical system, each sample was immersed and measured for 15 h in open circuit potential (OCP). During the OCP measurements, electrochemical impedance spectroscopy (EIS) was carried out under potentiostatic conditions at 1, 5, 10 and 15 h. The EIS measurements were performed over frequency range from 40 kHz to 6 mHz with an amplitude of ± 10 mV. After impedance measurements, potentiodynamic polarisation tests were performed on the same sample without removing the specimen from the cell. The polarisation tests were realised by scanning of the applied potential (E) from -700 $mV_{Ag/AgCl}$ and moving in the anodic direction to 1500 $mV_{Ag/AgCl}$ to the OCP at a rate of $1\ mV.s^{-1}$. The results were used to construct Tafel slopes plots in both anodic and cathodic domains. The corrosion potential E_{corr} and corrosion current i_{corr} were determined from the intersection of these two slopes plots. The test was terminated automatically when the current exceeded value of 1 mA. Each experiment

was repeated three times and the average values of electrochemical parameters were determined.

2.5. X-ray photoelectron spectroscopy (XPS)

The surface chemistry of the laser sintered sample in addition to specimens that were removed from the cell after 15 h of the electrochemical impedance spectroscopy (EIS) tests was characterised using XPS technique. Prior to the measurement, the specimens were rinsed with distilled water and blow-dried. Then, the samples were inserted into the XPS ultra-high vacuum chamber operating at 10^{-9} mbar. The XPS characterisation was performed with a SPECS Phoibos 150 hemispherical analyser with multi channeltron detection using X-ray Al-K_α anode. The XPS spectra were measured in two different polar emission angles $\theta = 0^\circ$ (normal emission) and $\theta = 60^\circ$ in order to extract film thickness. The data obtained were fitted using a Shirley background and Lorentzian peaks numerically convoluted with a normalised Gaussian function to describe instrumental broadening. The passive film thickness was determined using a simple dumping model to describe the signal attenuation of Cr 2p.

3. Results and discussion

The chemical composition of the laser sintered CoCrMo alloy obtained by x-ray fluorescence is given in Table 1.

3.1. Microstructural characterisation

Fig. 1 shows the X-ray diffraction profiles of precursor powder in addition to laser sintered samples prepared by electropolishing and grinding. Diffraction pattern analysis of both the precursor powder and the electropolished sample revealed presence of face-centered cubic (FCC) γ phase ICSD card # 52934 with nominal lattice parameter of 3.5688 Å. The determined lattice parameter using the three diffraction peaks in Fig. 1 was 3.578 Å. It is to be noted, that no other phase was detected in this condition or the volumetric fraction of the second phase is bellow the detection limit of the instrument (~5 vol.-%). In contrast, a mixture of γ and hexagonal close-packed (HCP) ε phase ICSD card # 53806 with nominal lattice parameters a = 2.514 Å and c = 4.105 Å was identified in the specimen after grinding. The determined lattice parameters of the ε phase were a = 2,544 Å and c = 4,126 Å. The presence of ε phase is attributed to γ → HCP ε strain-induced martensitic transformation caused by deformation of the near-surface layer during grinding [17].

Fig. 2 shows a low magnification SEM secondary-electron micrograph after electropolishing where fine cellular dendritic microstructure, grain boundaries in addition to laser tracks can be seen. The interdendritic spacing is approximately 1 μm. The cellular dendrites are not confined by the weld pool and in general intersect the weld pool boundaries. A presence of cellular dendrites is caused by fast cooling rate during solidification of the molten metal during the build process and is consistent with observations in ref. [18].

Fig. 3(a) shows a high magnification SEM secondary-electron micrograph of the laser sintered specimen. The energy dispersive spectroscopy (EDS) elemental mapping was performed in the boxed region shown in Fig. 3(a) for elements Co, Cr, Mo and Si. The EDS maps are presented in the bottom part of the Fig. 3 and results revealed a microsegregation of some elements (in particular Co) in interdendritic regions. Point analysis in the interdendritic regions showed that there is

Table 1
Chemical composition of the CoCrMo alloy.

Element	Co	Cr	Mo	Si	Mn	Fe	Ni
(wt-%)	63.45	28.14	6.91	0.65	0.72	0.08	0.05

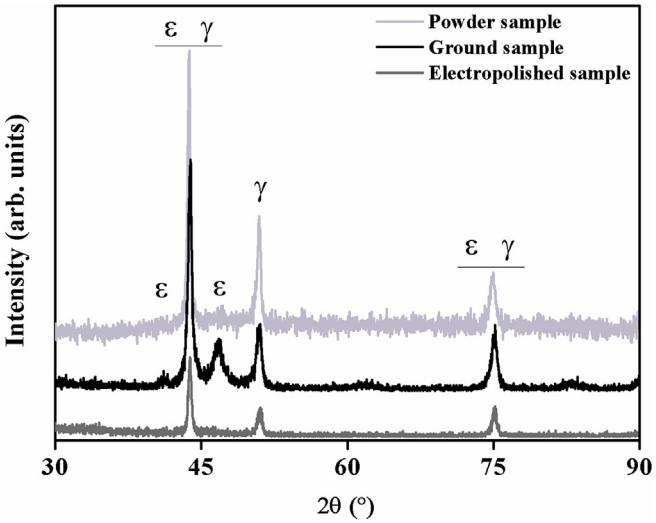

Fig. 1. X-ray diffraction patterns of the precursor powder and laser sintered samples subjected to electropolishing and grinding, respectively.

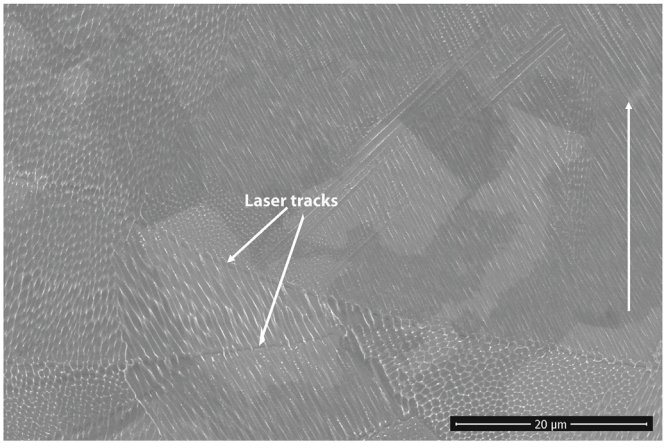

Fig. 2. Low magnification SEM secondary-electron micrograph of the laser sintered specimen revealing grains, cellular dendrites and laser tracks. The vertical arrow indicates the build direction.

concentration gradient of the main alloying elements when compared to the bulk chemical composition. The Co content showed a decrease from 63.2 wt.-% ± 0.4 from bulk composition to 58.4 wt.-% ± 0.6 in the interdendritic regions, indicating a Co enrichment of the dendrite core. For Cr, a marginal difference between bulk content and that in the interdendritic region was found, being 30.5 ± 0.3 and 29.5 wt.-% ± 0.4, respectively. Similarly, Mo enrichment of the interdendritic regions was found, reaching a concentration up to 6.9 wt.-% ± 0.3, which is higher than 5.3 wt.-% ± 0.5 of the bulk composition. This confirm a microsegregation from solid to liquid during solidification for Mo. Microsegregation of Mo was also observed in other alloys including Ni-based alloys [19,20]. In addition, Si also showed a microsegregation pattern similar to Mo, enriching the interdendritic regions. Its concentration increased to 0.86 wt.-% ± 0.05 in the interdendritic regions when compared to 0.6 wt.-% ± 0.1 of the bulk composition.

Although, it was possible to observe some inhomogeneity in chemical composition on the microscopic scale, the compositional difference between dendritic core and that in the interdendritic regions is considered to be low, especially for the alloying elements that contributes to corrosion resistance, in particular Cr and Mo. Thus, it can be assumed that even with the microsegregation occurring during the solidification, its effects on corrosion resistance of the CoCrMo alloy system can be considered as negligible.

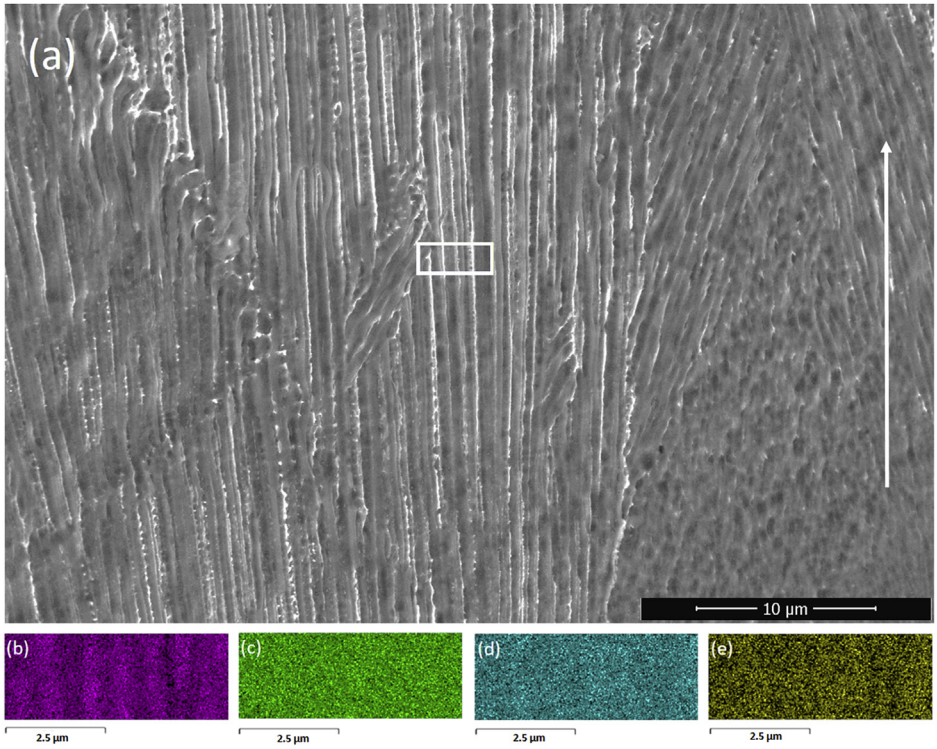

Fig. 3. (a) High magnification SEM secondary-electron micrograph of the laser sintered specimen. The vertical arrow indicates the build direction and the boxed region depicts area where EDS maps were acquired. EDS maps of (b) Co Kα; (c) Cr Lα; (d) Mo Lα; (e) Si Kα.

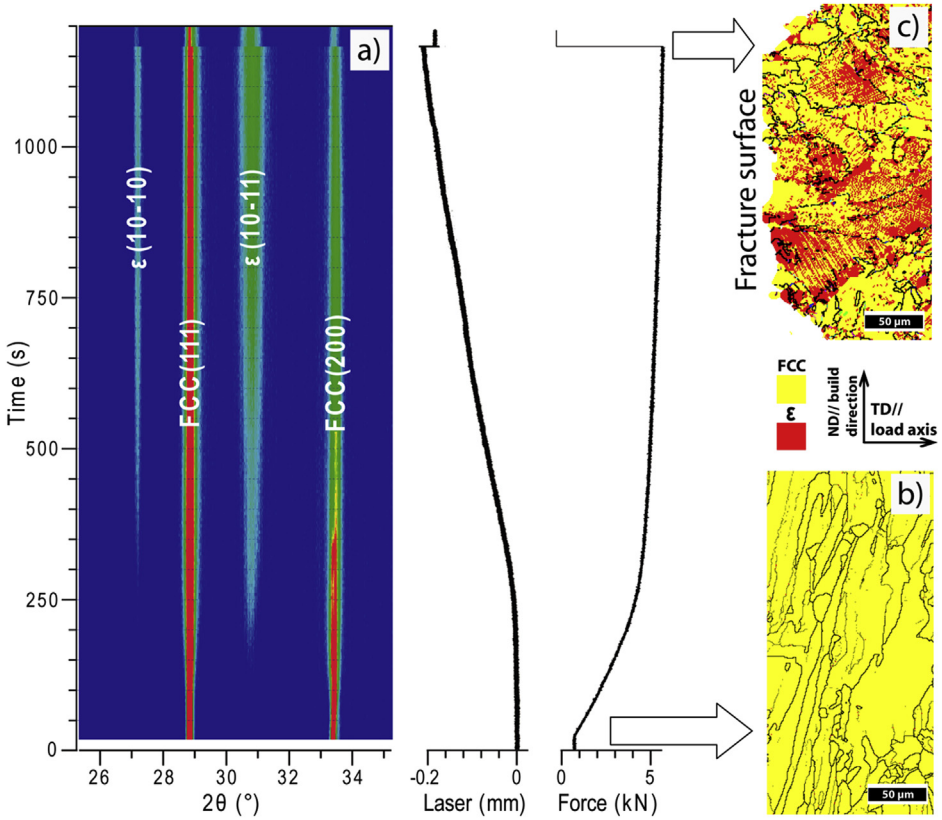

Fig. 4. (a) Left hand side, time-resolved synchrotron XRD data of the laser sintered sample subjected to tensile loading. The XRD data are plotted in an intensity colour map where dark blue corresponds to background counts and other colours are equivalent to counts intensity at the peak position with red being the maximum value. On the right hand side are presented corresponding values of the laser displacement and applied force, respectively. Fig. 4(b) presents EBSD phase map acquired prior to the straining showing FCC matrix with ~1 % volume fraction of ε HCP phase. An EBSD phase map collected close to the fracture of the deformed tensile test sample showing FCC phase with approximately ~40 % volume fraction of ε HCP phase, Fig. 4(c). In the EBSD maps, thick black lines represent high angle grain boundaries (misorientation greater than 10°), whereas thin black lines represent low angle grain boundaries (misorientation less than 2°). (For interpretation of the references to colour in this figure legend, the reader is referred to the Web version of this article.)

Fig. 4 illustrates the formation of HCP phase in the laser sintered sample subjected to tensile loading. The sample was deformed under tension to failure at a constant cross-head displacement rate of 10^{-3} mm.s^{-1} and simultaneously diffraction data were acquired. The time-resolved diffraction data are plotted in an intensity colour map, Fig. 4(a) (left hand side) together with corresponding values of laser displacement and applied force (right hand side). In the colour map, dark blue corresponds to background counts and other colours are

equivalent to counts intensity at the peak position with red being the maximum value. Prior to the loading, one can note a single-phase FCC structure as revealed by presence of two indexed FCC diffraction peaks. The subsequent straining causes FCC → ε HCP transformation as evidenced by appearance of additional ε (10–11) and ε (10-10) peaks at 160 and 250 s, respectively. The degree of transformation increases with progressing strain as indicated by change of colour intensity at the peak position.

The FCC → ε HCP transformation was further confirmed by EBSD analysis. Fig. 4(b) shows an EBSD phase map collected prior to the straining. In this map, a FCC matrix with ~1 % volume fraction of ε HCP phase (except for < 0.3 % non-indexed points) was identified. An EBSD phase map that was collected close to the fracture of the deformed tensile test sample is shown in Fig. 4(c). In this map, in addition to the FCC phase (highlighted by yellow colour), one can note plates of the ε HCP phase (highlighted by red colour). The volume fraction of the ε HCP phase determined by the EBSD analysis was almost 40 %. Therefore, the EBSD analysis combined with *in-situ* diffraction experiments evidenced the occurrence of strain-induced martensitic transformation in the alloy studied. This transformation is results of local change in the atomic stacking sequence of the ABC-type in the FCC phase which is altered to the hexagonal ABA-type by introducing stacking fault on every second {111} plane. The strain-induced martensitic transformation can contribute to enhancement of both the tensile strength and ductility in this alloy system due to suppression of necking and an increase in work-hardening rate by the martensite formation.

3.2. X-ray photoelectron spectroscopy (XPS)

The XPS survey revealed that the surface of the laser sintered sample is composed mainly of chromium and cobalt oxide, whereas predominantly metal signals from the bulk are present after sputtering of the surface in the XPS chamber, Fig. 5.

The XPS survey spectra recorded after electrochemical tests in four tested solutions show changes in the chemical composition on the sample surface, Fig. 6. In solutions containing albumin, the nitrogen signal shows a strong contribution located at ~400 eV, attributed to the presence of adsorbed protein on the metal surface.

In order to determine thickness of both passive film and adsorbed layer, the chromium spectrum was acquired at 0° and 60°. The XPS chromium spectrum measured at 0° and 60° in NaCl and

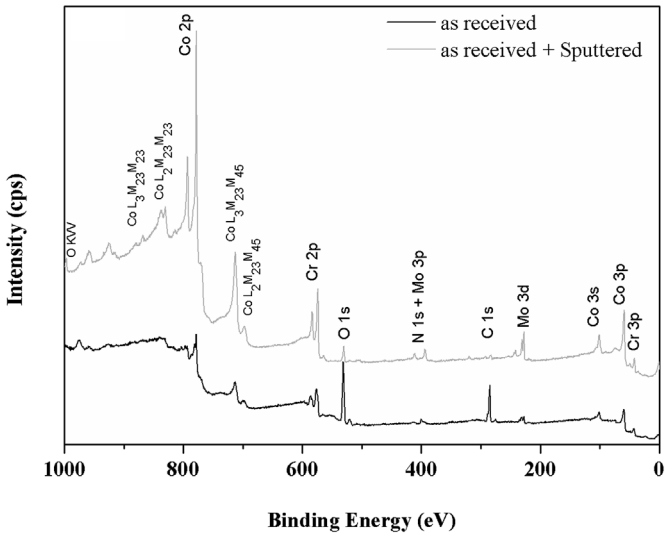

Fig. 5. Normalised XPS survey spectra of the laser sintered sample (black line) and after removing of the oxide layer (grey line) by sputtering in the XPS chamber revealing chemical composition on the sample surface.

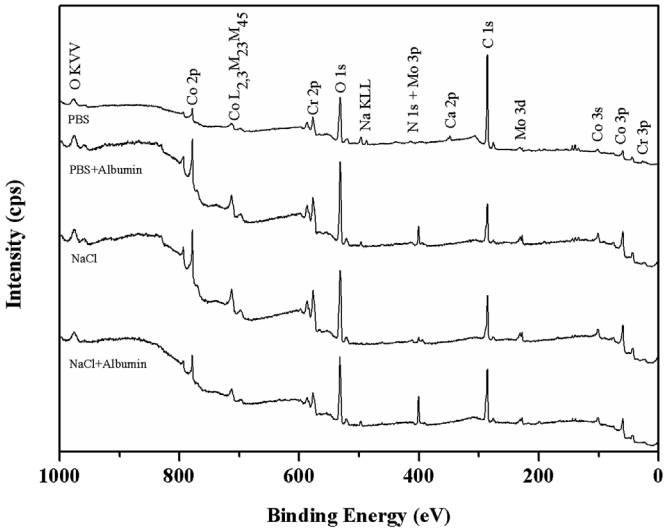

Fig. 6. Normalised XPS survey spectra recorded after electrochemical tests in four tested solutions.

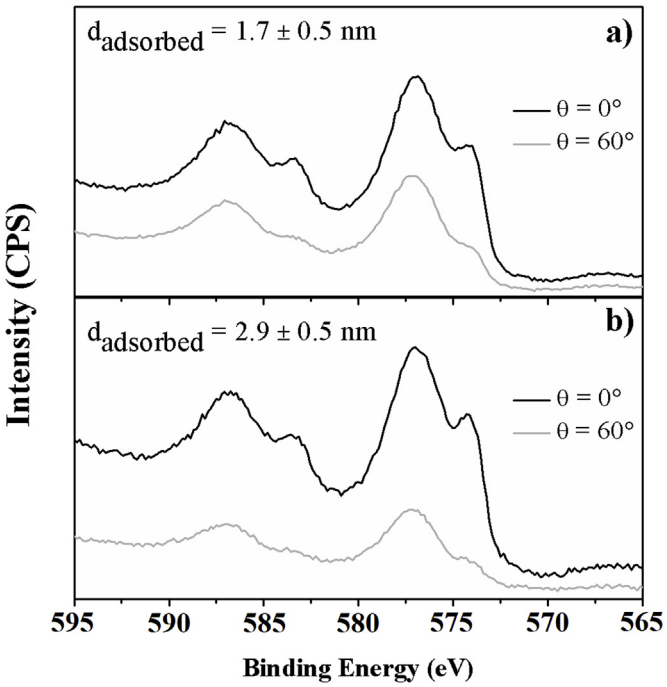

Fig. 7. XPS chromium spectrum measured at 0° and 60° after electrochemical test using solutions composed of a) NaCl and b) NaCl + albumin, revealing an increase in adsorbed film thickness (d_{adsorb}) in solution containing albumin.

Table 2
Peak area obtained from a simple fitting of Cr 2p considering only two components: a metallic one at 574.0 eV and that of oxide at 576.4 eV.

	Theta = 60°			Theta = 0°		
	Total	Metal	Oxide	Total	Metal	Oxide
NaCl	11711.7	821.2	10220	24164.5	4193	18803
NaCl + Albumin	3748	212	3271	12532.7	2363	9595
PBS + Albumin	10329	580	9042	21703	3868	16652

NaCl + albumin are presented in Fig. 7(a) and Fig. 7(b), respectively. An increase of adsorbed film thickness (d_{adsorb}) in solution containing albumin was observed.

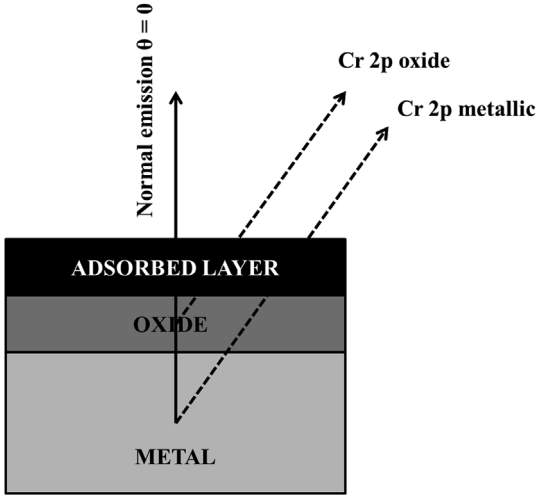

Fig. 8. A model of continuous thin films used for estimation of both the oxide and adsorbed film thickness.

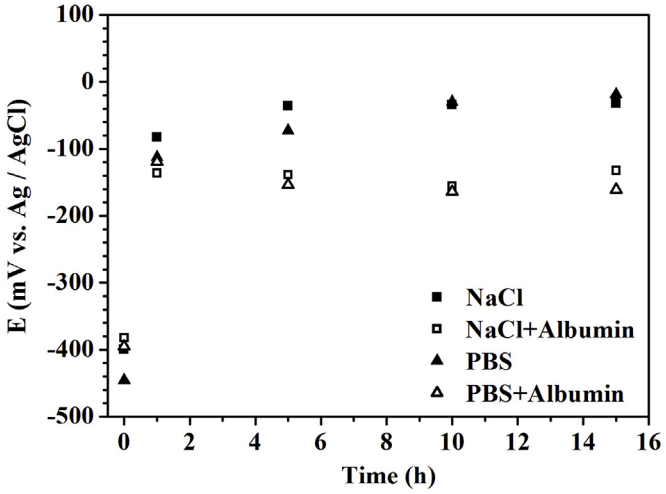

Fig. 9. OCP measurements recorded in NaCl and PBS solutions with and without albumin addition (tested at pH 7.4, 37 °C).

Table 2 shows peak area obtained from a simple fitting of Cr 2p considering only two components: a metallic one which is located at 574.0 eV and that of the oxide situated at 576.4 eV.

A simple model of continuous thin films, Fig. 8, to estimate the oxide and adsorbed film thickness was considered. The inelastic mean free-path λ_{adsorb} and λ_{ox} were calculated using the QUASES – IMFP software based on the TPP2M formula [21,22]. Using the signal from Cr 2p (I^{oxide} component) and solving equation (1) using two angles (0° and 60°) we can obtain thickness of the adsorbed film, d_{adsorb}. With this result, Cr 2p (I^{metal} component) can be used to extract the oxide film thickness from equation (2). The I_0 in the equations (1) and (2) is a constant intensity related to x-ray power, sample illumination and experimental geometry. The determined oxide film thickness is approximately 3.0 nm in all samples and the thickness of the adsorbed layer is about 1.7 nm in the NaCl solution whereas 2.9 nm in NaCl + Albumin and PBS + Albumin solutions.

$$I^{oxide}(\theta) = I_0 e^{\left(\frac{d_{adsorb}}{\lambda_{adsorb}\cos(\theta)}\right)} \quad (1)$$

$$I^{Metal}(\theta) = I_0 e^{\left(-\frac{d_{ox}}{\lambda_{ox}\cos(\theta)} - \frac{d_{adsorb}}{\lambda_{adsorb}\cos(\theta)}\right)} \quad (2)$$

Mo 3d was not considered because it has a very small intensity and for thick films, the obtained signal can be very low and therefore can compromise the measurement. Co 2p shows the strongest signal, which in principle could be an easy signal to be chosen. However, as observed in Fig. 5, there are several Auger transitions nearby the Co 2p peaks which could compromise the quantitative analysis. Moreover, Co 2p has the lowest kinetic energy compared to Cr 2p and Mo 3d, therefore for thick films and graze emission angles, it would be a challenging task to perform a proper measurement due to the strong signal dumping. On the other hand, Cr 2p electrons are emitted with intermediate kinetic energies, have large and well-resolved chemical shift between the oxide and metallic component, as well as a large photoemission cross-section. Thus, taking in account all experimental constraints, the best choice in our opinion is selection of Cr 2p.

3.3. Electrochemical tests

3.3.1. OCP measurements

Fig. 9 shows the OCP measurement as function of time. A continuous shifting of potential towards more positive values with progressing time is observed in solutions without albumin added. The positive potential evolution indicates a possible formation of a passivation layer on the sample surface. Comparing the two solutions with no albumin added the OCP values are higher for the NaCl solution until 5 h of measurement. After 5 h of immersion, the trend is inverted.

Albumin notably shifts the OCP towards more negative values when added in two solutions. For the albumin-containing solutions, the corrosion potential is nearly constant after 1 h of measurement. It is known that albumin may reduce cathodic reaction in CoCrMo alloys [23], thus shifting their OCP towards lower values. Vidal and Muñoz [3] showed that bovine serum albumin (BSA) addition into similar solutions resulted in OCP shift towards more negative values. This was related to the double role of BSA adsorption on the CoCrMo surface. The BSA adsorption on the one hand causes reduction of the cathodic reaction (impeding access of the oxidant to the metallic surface) and on the other hand increases the anodic reaction rate by forming soluble metal complexes. In addition, phosphate in PBS solution reduces the anodic reaction [24]. When both compounds are present in PBS solution, the albumin effect predominates.

Table 3 summarises the average values and standard deviation from the OCP measurements at time 0, 1, 5, 10 and 15 h of immersion.

3.3.2. Polarisation curves

Polarisation curves of CoCrMo alloy in NaCl and PBS solutions with and without addition of albumin are shown in Fig. 10. There is a usual active-passive transition in all solutions. In the cathodic domain, albumin slightly decreases the current density in both solutions. This is in agreement with results reported by Vidal and Muñoz [25] where was claimed that albumin acts as a cathodic inhibitor.

The cathodic to anodic current transition was observed in potential range between -750 and -650 $mV_{Ag/AgCl}$ to solutions with addition of albumin and between -250 and -150 $mV_{Ag/AgCl}$ to solutions without addition of albumin. When comparing the two solutions without addition of albumin, phosphate ions can passivate metal surface. Therefore, these ions translate the corrosion potential to more positive values and decrease the current density. The presence of albumin shifts

Table 3
OCP values ($mV_{Ag/AgCl}$) with scatter bands.

	Solution tested			
Time (hours)	NaCl	NaCl + Albumin	PBS	PBS + Albumin
0	-399 ± 28	-382 ± 3	-446 ± 9	-395 ± 8
1	-83 ± 6	-136 ± 20	-113 ± 11	-120 ± 12
5	-36 ± 4	-139 ± 17	-73 ± 6	-154 ± 4
10	-34 ± 7	-156 ± 13	-30 ± 6	-164 ± 8
15	-32 ± 5	-132 ± 19	-29 ± 7	-161 ± 6

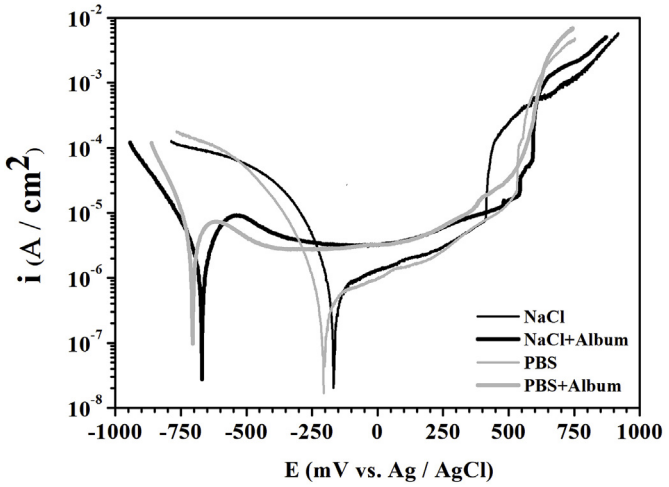

Fig. 10. Polarisation curves recorded in NaCl and PBS solutions with and without albumin addition (tested at pH 7.4, 37 °C).

Table 4
Potentiodynamic results with scatter bands of CoCrMo alloy in 0.14 NaCl and PBS with and without albumin addition (tested at pH 7.4, 37 °C).

Parameter	Solution tested			
	NaCl	NaCl + Albumin	PBS	PBS + Albumin
E_{corr} ($mV_{Ag/AgCl}$)	-164 ± 12	-674 ± 14	-201 ± 5	-700 ± 6
I_{corr} (μA/cm²)	0.56 ± 0.17	2.28 ± 0.92	0.33 ± 0.08	4.11 ± 0.83
E_{bp} ($mV_{Ag/AgCl}$)	414 ± 4	546 ± 6	539 ± 4	558 ± 5

the corrosion potential towards more negative values and increases the current density in both solutions. To facilitate comparison, the values of corrosion potential E_{corr}, corrosion current density i_{corr} and breakdown potential (transpassive region) E_{bp} were extracted from the polarisation curves and these are listed in Table 4. Tafel slop plots for NaCl and PBS solutions are presented in Fig. 11.

The active-passive plateau was observed in range from -700 up to 500 $mV_{Ag/AgCl}$ and from -200 up to 550 $mV_{Ag/AgCl}$ for solution with and without albumin addition, respectively. Addition of albumin increased both, the active-passive plateau and the current density. In solutions without addition of albumin, phosphate ions caused a drop in the current density.

In a stagnant solution, the metal surface ions can be released by ions of the solution through the dissolution process. As mentioned previously, stirring of solution was applied in the present work, which creates a turbulent flow on the sample surface. The amount of material reaching the metal surface increases by the mass transfer through the diffusion layer. Nevertheless, the metal ions and transport of oxygen to the surface required for the formation of the passive layer may decrease by convection process towards the bulk solution due to agitation. Therefore, the formation of the passive layer becomes more difficult. Even if formed, as indicated by a horizontal plateau of polarisation curves in the albumin-containing solutions, the passive layer will be thinner and possibly inhomogeneous than that formed under stagnant conditions [26].

The polarisation in the anodic direction in albumin containing solutions causes electron depletion, which favours the adsorption of negatively charged ions and molecules. The isoelectric point of albumin is 4.9 and in the test solutions that were adjusted to pH 7.4, the albumin will be negatively charged [8]. Therefore, albumin tends to form a film, which is adsorbed on the sample surface [3]. The more positive potentials and longer times for breakdown of the passive layer in albumin containing solutions can be explained in following way: since protein and chloride in both PBS and NaCl solution are negatively charged, they will compete to adsorb on the surface. Thus, the adsorption would retard the film breakdown [27].

Phosphate containing solutions with and without addition of albumin show a shoulder at approximately 400 and 350 $mV_{Ag/AgCl}$, respectively. Similar effect was reported in an electrolyte containing phosphates and it was attributed to the formation of phosphate-chromium ions complexes that activates transpassive dissolution [27]. The increase in the current at the end of the active-passive region can be caused by the dissolution of the chromium oxide in addition to water oxidation [28]. Therefore, albumin acts as cathodic inhibitor and can accelerate the anodic reaction, which is in good agreement with results of Vidal and Muñoz [27].

3.3.3. Electrochemical impedance spectroscopy (EIS)

The electrochemical behaviour in the metal/electrolyte interface and the adsorption process of albumin on the surface of CoCrMo alloy were examined by means of EIS measurements.

Fig. 12 shows the Nyquist diagrams after 1, 5, 10 and 15 h of immersion time at OCP in NaCl and PBS solutions with and without addition of albumin. In these diagrams it is possible to observe the formation of one capacitive semicircle. This is characteristic for charge transfer process at the metal/electrolyte interface. In Fig. 12, diameter of the semicircles increases with progressing immersion time in all tested solutions. It is known that CoCrMo alloys spontaneously form a thin oxide layer [29] in particular Cr_2O_3, which present both the chemical and physical barrier for the ion exchange [2]. Therefore, oxide

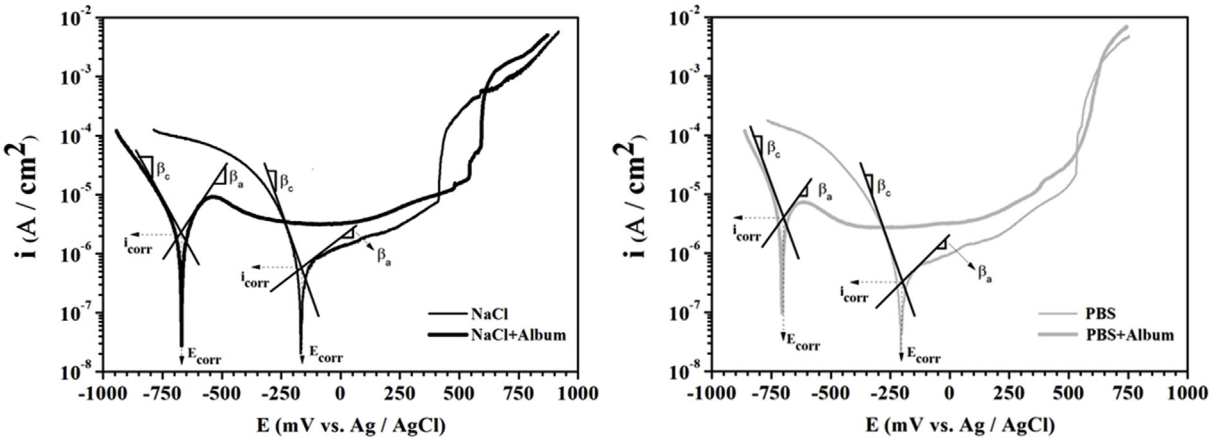

Fig. 11. Polarisation curves with Tafel slops plots for NaCl and PBS solutions with and without albumin addition (tested at pH 7.4, 37 °C).

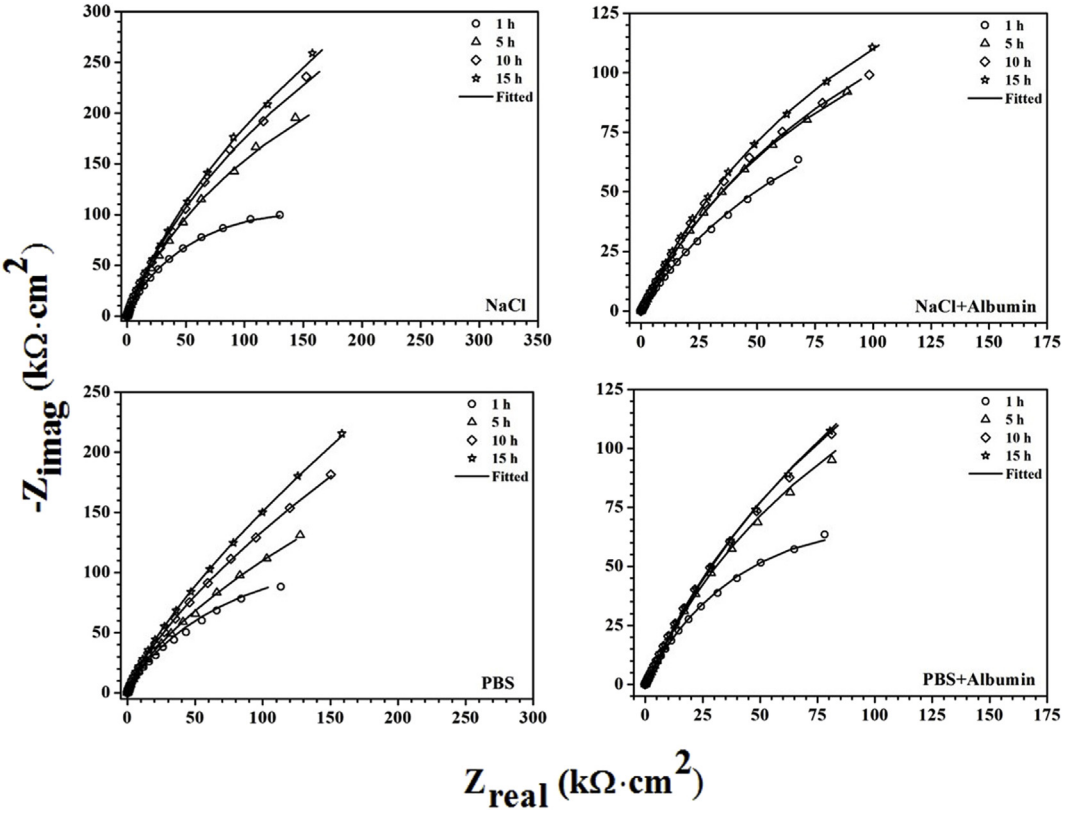

Fig. 12. Nyquist plots with fitted curves after 1, 5, 10 and 15 h of immersion time at OCP in NaCl and PBS solutions with and without addition of albumin (tested at pH 7.4, 37 °C).

layer would form capacitive semicircle at low frequencies in the Nyquist diagram. Charge transfer process through the electric double layer can result in second capacitive semicircle at high and medium frequencies [3,30]. However, only one capacitive semicircle was observed in Fig. 12.

Nyquist diagrams present limitation for separation of possible processes occurring at the metal/electrolyte interface. Bode diagrams are best suited to represent the separation due to the fact, that they show change of impedance as function of applied frequency.

Bode phase plots of electrochemical system with addition of albumin, Fig. 13, clearly shows two phase angles maxima which corresponds to two time constants. This indicates occurrence of two reactions with different kinetics [6]. The separation between the two-phase angles maximum is not well pronounced in NaCl and PBS solutions without addition of albumin.

The absolute impedance curve is almost constant at high frequencies (range from 10^5 up to 10^4 Hz). The phase angle is approximately 15° in this frequency range. This frequency range showed a resistive behaviour corresponding to the solution resistance between the working and the reference electrode. At frequency range of 60-10 Hz the first phase angle reached maximum values in approximately 80°. In this frequency range, the metal samples examined showed capacitive behaviour [31]. In addition, the second phase angle with maximum value at approximately 60° at frequency range of 1-0.05 Hz. The absolute impedance increased and the phase angle was shifted to the lower values in frequency range from 10 to 0.006 Hz in all solutions.

The metal/electrolyte interface, in addition to formation of oxide film and adsorbed albumin can be schematically represented by Randles model of equivalent electrical circuit (EEC) [3,30], which is shown in Fig. 14 in the bottom part of the figure. Two resistor-capacitor (RC) groups were used and the circuit description code was [([(RC)R]C)R]. The NOVA software v.1.11.0 was used for fitting of the EEC. It is to be noted that each of the RC group corresponds to the interfaces shown in the upper part of the figure.

The RC1 group is intercalated after the diffusion resistance (R_s) of ions from the bulk solution until these reach the Helmholtz external interface of the electrical double layer. This group is observed at frequencies between 10 and 10^3 Hz and represents the presence of inhomogeneous oxide film and the passive dissolution of this layer at the oxide film/electrolyte interface, *i.e.* the electrical double layer. The RC1 group consists of first constant phase element (CPE1) that represents the capacitance of the double layer C_{dl} in addition to R1 which represent the charge transfer resistance R_{ct} through this interface. The RC2 group is observed at frequencies between 10^{-2} and 1 Hz and represents the oxide film formation on the metal surface. This includes second constant phase element (CPE2) which consists of capacitance of the oxide film C_f in addition to R2 polarisation resistance of the system R_p. Similar considerations were reported by Huković and Babić [4].

Surface roughness, impurities, dislocations or grain boundaries of the sample leads to a non-ideal behaviour of the capacitive components [25]. Therefore, pseudo capacitors of both double layer C_{dl} and oxide film C_f need to be considered and these are represented by CPEs in Fig. 14. The NOVA software include fitting and simulation tool that simplify a parallel combination of a resistor and the CPE by converting it to pseudo capacitance according to equation (3):

$$C_{pseudo} = Y_0^{\frac{1}{n}} \cdot R^{\left(\frac{1}{n}-1\right)} \quad (3)$$

Where C_{pseudo} is the resulting pseudo capacitance, Y_0 is the admittance value of the CPE, R is the resistance value and n is the exponent of the CPE.

Using the EEC model, the experimental impedance data were fitted. A good agreement between the predicted (fitted lines) and measured data was found, Figs. 12 and 13. In these figures, both Nyquist and Bode diagrams for NaCl and PBS solutions with and without albumin addition are shown. Two-phase angles maxima in the fit confirmed, that

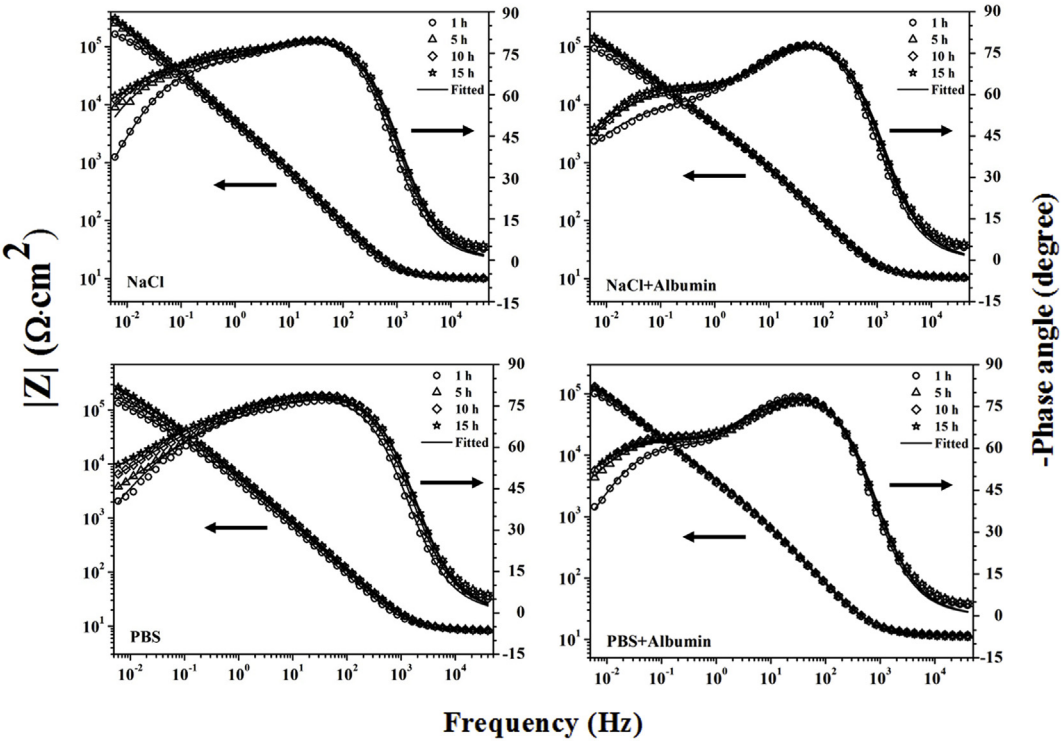

Fig. 13. Bode modulus and Bode phase plots with fitted curves after 1, 5, 10 and 15 h of immersion time at OCP in NaCl and PBS solutions with and without addition of albumin (tested at pH 7.4, 37 °C).

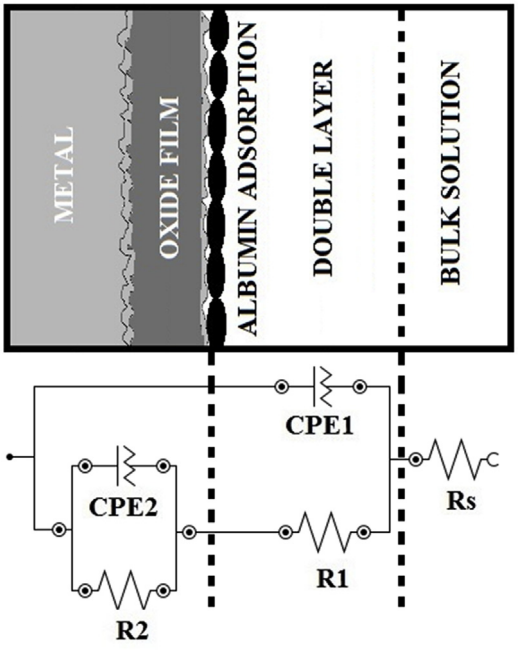

Fig. 14. Schematic representation of metal/electrolyte interface (upper part of the figure) and Randles equivalent circuit type [([(RC)R]C)R] shown in the bottom part of the figure. Rs is solution resistance, CPE1 represents capacitance of the double layer, R1 is charge transfer resistance, CPE2 represents capacitance of the oxide film and R2 is polarisation resistance of the system. Adapted from ref. [25].

in the analysed system, two electrochemical processes with different kinetics take place. Following the EEC model, electrical circuit parameters were calculated and results obtained are shown in **Table 5**.

The C_{dl} capacitance shows a gradual decrease with progressing time in all solutions. Similar results were obtained for forged CoCrMo alloys in simulated body fluids. Drop of the C_{dl} can be related to the charge separation on the double layer at the interface oxide film/electrolyte. This separation is caused by redox reaction and/or intercalation of the oxide film with adsorbed ions or molecules from the solution that results in an irreversible Faradaic charge transfer on the sample surface [32].

The influence of immersion time on the charge transfer resistance (R_{ct}) depends on the solution chemistry. In the NaCl solution, albumin increases the R_{ct} due to the barrier effect (adsorption) of the protein molecules. However, this effect is reduced with progressing time because formation kinetic and properties of the passive film changes with the applied potential. Also, adsorption properties of the albumin on the oxide film depend on the electrostatic force, which changes with variation of the electrical potential. In addition, the mass transfer through the diffusion layer increases with stirring and consequently influences the formation of the passive layer. When formed, this layer is thinner and may presents discontinuities and consequently reduces the charge transfer resistance [26]. Albumin reduces the R_{ct} when present in the PBS solution. With progressing OCP time, albumin modify the electrochemical properties of the passive film which is in line with results reported by Muñoz and Mischler [33]. They claimed that the presence of the protein displaces the phosphate ions inhibiting the protective effect of phosphates. In ref. [3], higher R_{ct} values in PBS solutions without addition of albumin were attributed to the fact that the phosphate ions formed a layer on the electrode surface. This phosphate ion barrier hinders the mass transport of oxygen and/or of reaction products to and/or from the electrode surface. Albumin is less efficient in reducing the reaction rate because larger size of its molecules does not allow the formation of the compact film [27].

The presence of albumin increases the capacitance of the oxide film (C_f) in NaCl solution. However, in the NaCl solution-containing albumin, C_f decreases after the first hour of immersion and remains almost constant between 5 and 15 h of OCP. In the PBS solutions with and without addition of albumin, C_f increases with progressing time. Similar

Table 5
Electrical circuit parameters with scatter bands obtained from the EEC model (tested at pH 7.4, 37 °C).

		OCP time (hours)			
		1	5	10	15
Solution tested	Parameter				
NaCl	$R_s(\Omega)$	42.8 ± 2.20	42.50 ± 2.10	42.2 ± 2.60	41.90 ± 2.50
	C_{dl} (μF.cm^{-2})	4.42 ± 0.11	3.73 ± 0.15	3.45 ± 0.12	3.35 ± 0.14
	R_{ct} (kΩ.cm^2)	2.24 ± 0.30	2.54 ± 0.20	2.43 ± 0.50	2.63 ± 0.60
	C_f (μF.cm^{-2})	13.60 ± 1.20	19.90 ± 1.50	20.70 ± 2.20	22.3 ± 1.70
	R_p (MΩ.cm^2)	1.25 ± 0.15	3.51 ± 0.12	5.31 ± 0.11	6.91 ± 0.10
NaCl + Albumin	$R_s(\Omega)$	47.00 ± 2.50	46.20 ± 2.40	45.60 ± 2.30	45.10 ± 2.10
	C_{dl} (μF.cm^{-2})	3.58 ± 0.13	3.19 ± 0.17	3.14 ± 0.12	3.10 ± 0.27
	R_{ct} (kΩ.cm^2)	18.50 ± 1.10	14.70 ± 0.20	11.80 ± 0.40	11.60 ± 1.80
	C_f (μF.cm^{-2})	77.00 ± 3.10	47.20 ± 6.20	46.30 ± 8.20	48.10 ± 4.60
	R_p (MΩ.cm^2)	1.21 ± 0.06	1.55 ± 0.10	1.66 ± 0.17	1.83 ± 0.14
PBS	$R_s(\Omega)$	43.90 ± 2.50	43.30 ± 2.10	42.90 ± 2.00	42.70 ± 2.10
	C_{dl} (μF.cm^{-2})	3.11 ± 0.21	2.63 ± 0.27	2.48 ± 0.31	2.42 ± 0.34
	R_{ct} (kΩ.cm^2)	16.30 ± 2.10	16.50 ± 1.50	21.80 ± 1.90	26.10 ± 1.20
	C_f (μF.cm^{-2})	21.70 ± 1.50	76.10 ± 6.80	71.30 ± 6.50	79.80 ± 6.10
	R_p (MΩ.cm^2)	1.43 ± 0.38	4.07 ± 0.27	7.12 ± 0.89	11.31 ± 0.79
PBS + Albumin	$R_s(\Omega)$	50.20 ± 3.70	49.10 ± 3.90	48.10 ± 4.20	47.50 ± 3.90
	C_{dl} (μF.cm^{-2})	3.69 ± 0.92	3.44 ± 0.90	3.46 ± 0.94	3.36 ± 0.90
	R_{ct} (kΩ.cm^2)	17.10 ± 1.80	14.30 ± 1.20	13.50 ± 1.40	13.30 ± 1.10
	C_f (μF.cm^{-2})	35.10 ± 1.60	40.20 ± 1.30	43.50 ± 1.20	51.20 ± 1.10
	R_p (MΩ.cm^2)	1.08 ± 0.32	1.41 ± 0.02	1.44 ± 0.02	1.52 ± 0.08

results were reported by Vidal and Muñoz [3]. When comparing PBS solution with and without addition of albumin, C_f values are lower in solution with addition of albumin except for the first hour of immersion.

A decrease of the C_f values in NaCl solution with addition of albumin can be associated with the increase in thickness of the passive layer due to the presence of the protein, in accordance of previous XPS results. C_f can be related to oxide film thickness approaching the dielectric behaviour of the parallel plate capacitor according to the following equation (4) [3,34]:

$$C_f = \frac{\varepsilon\varepsilon_0 A}{d} \tag{4}$$

Where ε is dielectric constant of the layer, ε_0 is the permittivity of free space (8.85×10^{-14} F.cm^{-1}), A the active area and d the oxide film thickness.

Considering *A is* constant, C_f depends both dielectric properties of the oxide film and its thickness, which may change with immersion time. Hodgson *et al.* [28], Vidal and Muñoz [27] studied at a fixed potential, the impedance spectra of a CoCrMo wrought alloy and they observed variations in both dielectric properties and thickness of the passive film with immersion time, thus supporting the previous statement. The CoCrMo surface oxides have a voltage-dependent impedance behaviour that reflects the properties of the passive-oxide film, such as changes in the thickness and chemistry of the oxide [35]. However, XPS results of Ithurbide *et al.* [36] revealed that an increase in both the passive potential and pH, the thickness of oxide and adsorbed layer remains constant and the passive film is not modified by the adsorption of the protein. Variations in the passive film properties, morphology and its composition can be attributed to adsorption of phosphate and albumin molecules on the metal surface [3,37].

In our work, XPS results revealed changes in chemical composition on the sample surface in the laser sintered condition and after electrochemical tests in four solutions. The determined oxide film thickness was approximately 3.0 nm in all samples tested. Therefore, the change of the dielectric properties of passive film in PBS solutions may influences to a greater extent the C_f when taking in account possible changes in the passive film thickness with progressing time.

Finally, when comparing the results of all solutions, polarisation resistance (R_p) increases with progressing time. This suggests a further stabilisation of the oxide film. The addition of albumin decreases the R_p values of the solutions tested and consequently decreases the corrosion resistance of the alloy. Highest R_p values were observed in the PBS solution without protein added. Therefore, highest corrosion resistance is expected in this condition, because of precipitation of phosphate ions on the sample's surface. The values of R_p obtained from EIS are consistent with polarisation curves data, **Fig. 10**. Similar results were reported by Vidal and Muñoz [27] for CoCrMo wrought alloy for longer periods of exposure. They concluded that immersion time above 15 h modifies the surface behaviour of the material increasing the corrosion resistance of the oxide film mainly in the phosphate-containing solutions while decreasing the corrosion resistance in the albumin-containing solutions.

The EBSD analysis also revealed anisotropy in crystallographic orientation consistent with results reported in ref. [18] which can lead to inhomogeneous corrosion properties. For example, the (111) close-packed crystallographic planes in the FCC lattice of CoCrMo alloys typically exhibit a higher corrosion resistance. This is due to the fact that the higher atomic coordination and stronger atomic bonds in these planes causes a decrease of the surface energy which in turn increases the corrosion resistance of the alloy [38]. In this paper, the anisotropy in grain orientation was found to have less significant effects on corrosion resistance compared to the precipitation behaviour and grain boundaries characteristics. The later can lead to initiation of localised corrosion in corrosive solutions.

In the present work, we have examined the effect of the electrolyte composition on the corrosion behaviour and the influence of anisotropy on the corrosion rate was not accounted for. In this regard, the microstructure was considered to be identical for all tests. A systematic analysis of the relationship between crystallographic orientation and the corrosion behaviour will be the subject of our future research.

Experimental data obtained in our study can be used to improve accuracy of numerical models [39,40].

4. Conclusions

Corrosion behaviour and the surface chemistry of biomedical CoCrMo alloy produced by direct metal laser sintering technique was assessed during electrochemical tests conducted in different mediums. Mediums included 0.14 M NaCl and phosphate buffered solutions (PBS) both with and without addition of albumin. The influence of solution chemistry and immersion time on the electrochemical behaviour was evaluated using electrochemical impedance spectroscopy in addition to potentiodynamic tests. X-ray photoelectron spectroscopy was employed to study both passive film and adsorbed layer after electrochemical tests. In addition, a microstructural analysis was performed.

From the work conducted, the following conclusions can be drawn:

- Among four different tested solutions, the highest corrosion resistance (Rp values) after 15 h of immersion was observed in the order of PBS > NaCl > NaCl + albumin > PBS + albumin.
- The corrosion behaviour of the laser sintered material in solutions tested is comparable to a conventionally produced cast and/or forged alloy.
- The solidification microstructure and microsegregation that develops during the DMLS process does not impair the corrosion resistance of the alloy.
- The chemical composition and thickness of the passive film is not modified by the adsorbed layer.
- Microstructural and XRD analysis revealed occurrence of strain-induced martensitic tranformation, that contributes to an enhancement of alloy strength and the ductility.

Acknowledgements

The authors are grateful F.L. Bernardes for fabrication of the samples. Experimental support of L.H.M. Antunes at Unicamp, Campinas in addition to Mr. L. Wu, Dr. F.E. Montoro and Dr. A.L. Gobbi (projects ME 22425 and LMF 20869) at Brazilian Nanotechnology National Laboratory-LNNano is acknowledged. The authors acknowledge the LNNano and the Brazilian Synchrotron Light Laboratory-LNLS for the use of the XTMS installation at the XRD-1 beamline. Microstructural characterisation was performed at Analytical Centre - UFC/CT-INFRA/MCTI-SISNANO/Pró-Equipamentos CAPES and LNNano. Financial support was provided by CAPES, Brazil (Project 50/2011), CNPEM, Brazil (Project 20170618) and the São Paulo Research Foundation FAPESP, Brazil (grant numbers 2016/09350-2 and 2007/54829-5).

References

[1] H.C. Amstutz, P. Grigoris, Metal on metal bearings in hip arthroplasty, Clin. Orthop. Relat. Res. (1996) 11–34.
[2] S. Zangeneh, H.R. Lashgari, A. Roshani, Microstructure and tribological characteristics of aged Co – 28Cr – 5Mo – 0 . 3C alloy, Mater. Des. 37 (2012) 292–303.
[3] C.V. Vidal, A.I. Muñoz, Study of the adsorption process of bovine serum albumin on passivated surfaces of CoCrMo biomedical alloy, Electrochim. Acta 55 (2010) 8445–8452.
[4] M. Metikoš-Huković, R. Babić, Passivation and corrosion behaviours of cobalt and cobalt-chromium-molybdenum alloy, Corros. Sci. 49 (2007) 3570–3579.
[5] F. Contu, B. Elsener, H. Bo, Corrosion behaviour of CoCrMo implant alloy during fretting in bovine, serum 47 (2005) 1863–1875.
[6] A.I. Muñoz, J. Schwiesau, B.M. Jolles, S. Mischler, In vivo electrochemical corrosion study of a CoCrMo biomedical alloy in human synovial fluids, Acta Biomater. 21 (2015) 228–236.
[7] S. Karimi, T. Nickchi, A.M. Alfantazi, Long-term corrosion investigation of AISI 316L, Co-28Cr-6Mo, and Ti-6Al-4V alloys in simulated body solutions, Appl. Surf. Sci. 258 (2012) 6087–6096.
[8] S. Karimi, A.M. Alfantazi, Ion release and surface oxide composition of AISI 316L, Co-28Cr-6Mo, and Ti-6Al-4V alloys immersed in human serum albumin solutions, Mater. Sci. Eng. C 40 (2014) 435–444.
[9] D.R. Haynes, S.D. Rogers, S. Hay, M.J. Pearcy, D.W. Howie, The differences in toxicity and release of bone-resorbing mediators induced by titanium and cobalt-chromium-alloy wear particles, J. Bone Joint Surg. Am. 75 (1993) 825–834.
[10] T.P. Schmalzried, P.C. Peters, B.T. Maurer, C.R. Bragdon, W.H. Harris, Long-duration metal-on-metal total hip arthroplasties with low wear of the articulating surfaces, J. Arthroplast. 11 (1996) 322–331.
[11] W.E. Frazier, Metal additive manufacturing: a review, J. Mater. Eng. Perform. 23 (2014) 1917–1928.
[12] E. Liverani, A. Fortunato, A. Leardini, C. Belvedere, S. Siegler, L. Ceschini, A. Ascari, Fabrication of Co – Cr – Mo endoprosthetic ankle devices by means of Selective Laser Melting (SLM), JMADE 106 (2016) 60–68.
[13] M. Seifi, A. Salem, J. Beuth, O. Harrysson, J.J. Lewandowski, Overview of materials qualification needs for metal additive manufacturing, JOM (2016) 1–18.
[14] Y. Lu, S. Wu, Y. Gan, J. Li, C. Zhao, D. Zhuo, J. Lin, Investigation on the microstructure, mechanical property and corrosion behavior of the selective laser melted CoCrW alloy for dental application, Mater. Sci. Eng. C 49 (2015) 517–525.
[15] S.S. Babu, E.D. Specht, S.A. David, E. Karapetrova, P. Zschack, M. Peet, H.K.D.H. Bhadeshia, In-situ observations of lattice parameter fluctuations in Austenite and transformation to bainite, Metall. Mater. Trans. A 36 (2005) 3281–3289.
[16] A.I. Muñoz, S. Mischler, Effect of the environment on wear ranking and corrosion of biomedical CoCrMo alloys, J. Mater. Sci. Mater. Med. 22 (2011) 437–450.
[17] K. Yamanaka, M. Mori, Y. Koizumi, A. Chiba, Local strain evolution due to athermal γ→ε martensitic transformation in biomedical CoCrMo alloys, J. Mech. Behav. Biomed. Mater. 32 (2014) 52–61.
[18] A. Takaichi, Suyalatu, T. Nakamoto, N. Joko, N. Nomura, Y. Tsutsumi, S. Migita, H. Doi, S. Kurosu, A. Chiba, N. Wakabayashi, Y. Igarashi, T. Hanawa, Microstructures and mechanical properties of Co-29Cr-6Mo alloy fabricated by selective laser melting process for dental applications, J. Mech. Behav. Biomed. Mater. 21 (2013) 67–76.
[19] E.M. Miná, Y.C. da Silva, J. Dille, C.C. Silva, The effect of dilution on microsegregation in AWS ER NiCrMo-14 alloy welding claddings, Metall. and Mat. Trans. A 47 (2016) 6138–6147.
[20] C.C. Silva, H.C. Miranda, M.F. Motta, J.P. Farias, C.R.M. Afonso, A.J. Ramirez, New insight on the solidification path of an alloy 625 weld overlay, J. Mater. Res. Tech. 2 (2013) 228–237.
[21] S. Tanuma, C.J. Powell, D.R. Penn, Calculations of electron inelastic mean free paths. V. Data for 14 organic compounds over the 50–2000 eV range, Surf. Interface Anal. 21 (1994) 165–176.
[22] H. Shinotsuka, S. Tanuma, C.J. Powell, D.R. Penn, Calculations of electron inelastic mean free paths. X. Data for 41 elemental solids over the 50eV to 200keV range with the relativistic full Penn algorithm, Surf. Interface Anal. 47 (2015) 871–888.
[23] S. Hiromoto, E. Onodera, A. Chiba, K. Asami, T. Hanawa, Microstructure and corrosion behaviour in biological environments of the new forged low-Ni Co-Cr-Mo alloys, Biomaterials 26 (2005) 4912–4923.
[24] T. Hanawa, S. Hiromoto, K. Asami, Characterization of the surface oxide film of a Co-Cr-Mo alloy after being located in quasi-biological environments using XPS, Appl. Surf. Sci. 183 (2001) 68–75.
[25] C.V. Vidal, A.I. Muñoz, Electrochemical aspects in biomedical alloy Characterization : electrochemical impedance spectroscopy, Biomed. Eng. Trends Mater. Sci. (2011) 283–306.
[26] B. Poulson, Advances in understanding hydrodynamic effects on corrosion, Corros. Sci. 35 (1993) 655–661.
[27] C.V. Vidal, A.I. Muñoz, Electrochemical characterisation of biomedical alloys for surgical implants in simulated body fluids, Corros. Sci. 50 (2008) 1954–1961.
[28] A.W.E. Hodgson, S. Kurz, S. Virtanen, V. Fervel, C.O.A. Olsson, S. Mischler, Passive and transpassive behaviour of CoCrMo in simulated biological solutions, Electrochim. Acta 49 (2004) 2167–2178.
[29] M. Metikoš-Huković, R. Babić, Some aspects in designing passive alloys with an enhanced corrosion resistance, Corros. Sci. 51 (2009) 70–75.
[30] A. Kocijan, I. Milošev, D.K. Merl, B. Pihlar, Electrochemical study of Co-based alloys in simulated physiological solution, J. Appl. Electrochem. 34 (2004) 517–524.
[31] C. Vasilescu, S.I. Drob, J.M.C. Moreno, P. Osiceanu, M. Popa, E. Vasilescu, M. Marcu, P. Drob, Long-term corrosion resistance of new Ti – Ta – Zr alloy in simulated physiological fluids by electrochemical and surface analysis methods, Corros. Sci. 93 (2015) 310–323.
[32] P. Kurzweil, Electrochemical double-layer capacitors, Electrochem. Energy Storage Renew. Sources Grid Balanc, 2014, pp. 345–407.
[33] A.I. Muñoz, S. Mischler, Interactive effects of albumin and phosphate ions on the corrosion of CoCrMo implant alloy, J. Electrochem. Soc. 154 (2007) C562.
[34] P. Bommersbach, C. Alemany-Dumont, J.P. Millet, B. Normand, Formation and behaviour study of an environment-friendly corrosion inhibitor by electrochemical methods, Electrochim, Acta 51 (2005) 1076–1084.
[35] M. Haeri, S. Goldberg, J.L. Gilbert, The voltage-dependent electrochemical impedance spectroscopy of CoCrMo medical alloy using time-domain techniques : Generalized Cauchy – Lorentz, and KWW – Randles functions describing non-ideal interfacial behaviour, Corros. Sci. 53 (2011) 582–588.
[36] A. Ithurbide, I. Frateur, A. Galtayries, P. Marcus, XPS and flow-cell EQCM study of albumin adsorption on passivated chromium surfaces: influence of potential and pH, Electrochim. Acta 53 (2007) 1337–1346.
[37] J.J. Gray, C.A. Orme, Electrochemical impedance spectroscopy study of the passive films of alloy 22 in low pH nitrate and chloride environments, Electrochim. Acta 52 (2007) 2370–2375.
[38] X. Gong, Y. Li, Y. Nie, Z. Huang, F. Liu, L. Huang, L. Jiang, H. Mei, Corrosion behaviour of CoCrMo alloy fabricated by electron beam melting, Corros. Sci. 139 (2018) 68–75.
[39] L. Novotný, Calculation of T – stress on 3D specimens with crack, Procedia Eng 48 (2012) 489–494.
[40] M. Halama, D. Jerolitsch, J. Žilková, R. Dzedzina, P. Linhardt, Improvement of ENA-NOCS Technique Using Artificial Neural Networks Approach for the Detection of Corrosion, Eurocorr 2010, MAKC Press, 2010, pp. 1–8.